Electro- and Thermo-Optics Response of X-Cut Thin Film LiNbO$_3$ Waveguides

Alessandro Prencipe[ID] and Katia Gallo

Abstract—**Lithium niobate has been for decades the material of election for integrated nonlinear and electro-optics. Its recent availability in thin films affording subwavelength confinement of light and nanostructuring capabilities has led to ground-breaking results in numerous applications, ranging from ultrafast signal processing to efficient nonlinear optics, where electro-optic (EO) and thermo-optic (TO) functionalities can be further leveraged for enhanced tunability and reconfigurability. This work provides a consistent comparison between these two approaches in the most widely used configuration in LiNbO3 nanophotonics at telecom wavelengths. Using state of the art Bragg grating technology for high precision index measurements, we evaluate the guided-wave EO and TO tunability to be 3×10^{-5} V^{-1} and 3.6×10^{-3} W^{-1}, respectively, and study further operation and design tradeoffs, cross-talk effects and long-term stability. The results provide useful insights to identify the most appropriate strategies for implementing reconfigurable integrated photonic circuits effectively leveraging the unique features of LiNbO3.**

Index Terms—**Photonic integrated circuits, lithium niobate on insulator, integrated bragg filter, electrooptics, thermooptics.**

I. Introduction

PHOTONIC integrated circuits (PICs) have become fundamental tools in a wide range of classical and quantum optics applications, due to the clear advantage they offer in terms of scalability, stability, footprint and low power consumption, with respect to tabletop counterparts [1], [2], [3], [4]. A highly desirable feature in the context of a great number of PIC applications is their electrical reconfigurability, meaning the possibility of statically tune the device, in a similar fashion to Ref. [5]. Besides allowing individual device trimming, this feature is the key enabler of core functionalities in PICs for neuromorphic computing [6], free-space transceiver [7], microwave photonics [8], datacenter interconnects [9], as well as quantum state tomography in discrete and continuous variable regimes [10].

A number of strategies can be used to implement on-chip tunability. Strain [11] and carrier injection [12], often

implemented in silicon photonics, may be limited by high power consumption and by additional optical losses [13]. On the other hand thermo-optic (TO) effects can effectively be leveraged on most PIC platforms with relatively low complexity and very stable performance over long time-scales [14]. However, they may suffer from cross-talk in densely-packed PIC configurations, and exhibit intrinsically lower speeds as well as relatively high power consumption in comparison to electro-optic (EO) devices based on the Pockels effect. Exploiting the latter in nanophotonic formats is particularly appealing, as it affords extremely high modulation speeds and reduced power consumption. However this is possible only for some photonic platforms, due to the required non-centrosymmetry of the underlying material.

Lithium niobate, by virtue of its EO properties, has been widely used for decades to implement high-speed optical modulators [15]. Recently, with the development of ultra-low loss optical circuits in thin film lithium niobate (TFLN) [16], such capabilities have been leveraged also in nanophotonic PIC formats [17], [18], [19], [20] and in the last few years, this new photonic platform has enabled a series of ground-breaking results also in nonlinear [21] and quantum optics [22], [23], [24].

On the other hand, EO devices in LN are known to exhibit an unstable behaviour over time, due to the so-called DC drift [25], [26]. This may be an obstacle for those applications in which stability is a critical issue and a feedback system is hard to implement. This scenario is extremely common, for example, in quantum optics during the implementation of a quantum tomography, when single photon signals are acquired for several hours to retrieve the density matrix of the quantum state under test [27] or during heterodyne detection in continuous variable quantum optics [28]. Long-term stability issues are also relevant in the context of classical applications, e.g. tunable spectral filtering, low-frequency switching and even in high-frequency modulators, imposing the need for active compensation of the drifting DC biases in LN waveguides [29] as well as in LN commercial devices. Such effects are naturally exacerbated in nanophotonic TFLN geometries, by the much higher electrical and optical field confinement. Therefore, additional TO controls are often embedded in EO PICs for critical applications [30], and in some cases they are even preferred to EO ones to implement specific functionalities in complex TFLN chips [29], [31], [32].

This article presents a comparative study of the electro-optic and thermo-optic static reconfigurability of optical waveguides
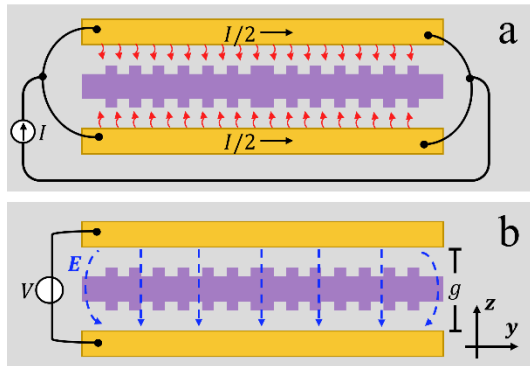
Fig. 1.   Schematic of the device tuned via (a) thermo-optic and (b) electro-optic effect with the y-z axes of LN. In the former case, the maximum tunability of the device is increased by the symmetric electrode configuration.

in thin film lithium niobate, relevant to the by far most common configuration for PICs in LN (using TE_{00} modes of nanophotonic rib waveguides with propagation along the y-axis in x-cut TFLN) accessing the largest EO coefficient of the material ($r_{33} = 31$ pm/V [17]) with coplanar electrode geometries [17], [18], [20]. We address EO and TO effects with experiments deliberately performed on devices with identical waveguides and electrode geometries, fabricated on the same substrate (500nm-thick commercial TFLN wafer) and undergoing the same fabrication process, in order to remove artefacts affecting comparisons across different designs, samples and fabrication conditions. To accurately characterize the TFLN guided-mode index changes we leveraged the exquisite sensitivity to refractive index changes afforded by integrated phase-shifted Bragg gratings (PSBG) embedded in the TFLN optical layer. This allowed us to accurately quantify index variations under the application of an external voltage $\mathcal{V}$ in static conditions: $\delta n = \delta n(\mathcal{V})$, in the EO mode of operation and when dissipating an electrical power $\mathcal{P}$ in the resistive microheater: $\delta n = \delta n(\mathcal{P})$, in the TO mode. In the following sections we provide an overview of the fabricated devices (Sect. II) and of the principle of operation of the integrated refractive index sensors (Sect. III). We then systematically compare the performance of TO and EO TFLN waveguides considering their electrical tunability (Sect. III-A), crosstalk (III-B), loss tradeoffs (III-C), maximum index modulation (III-D) and long-term stability (III-E). The results provide practical guidelines useful to identify the most appropriate strategies for achieving PIC reconfigurability in TFLN waveguides, while taking into account possibilities and limitations of its TO and EO capabilities, so to best fit the needs of the fast growing range of applications for this important nanophotonic platform.

II. DEVICE OVERVIEW

Fig. 1 provides an overall view of the thin film Lithium Niobate (TFLN) optical waveguide structures with their TO and EO control electrodes. To allow meaningful comparisons of TO and EO devices, all of them were implemented in pairs (often on the very same chip), using identical designs and fabrication conditions.

The devices were implemented in commercial x-cut congruent TFLN bonded to thermally oxidized Si carrier wafers (NanoLN Ltd), diced into individual chip sizes of 1.3×1cm². Densely packed integrated optical circuits consisting of 300 nm-high nanowire rib waveguides etched into 500 nm-thick LN layers were individually addressed by standard single-mode telecom optical fibers, using broadband grating structures for vertical off-chip coupling, embedded in the TFLN [33]. The thickness of the thermal SiO₂ separating the TFLN from the Si carrier wafer is 2μm.

The active part of each device consisted of a pair of control electrodes (marked in yellow in the device top-view of Fig.1) running in parallel to the optical guiding channel (in violet). To fit the most widely employed configuration for TFLN integrated optical devices, utilizing the largest nonlinear optical (d_{33}) and electro-optic (r_{33}) coefficients and accessing the thermo-optic effect [34] in x-cut LN, both electrodes and waveguides were aligned with the crystallographic y axis. The electrodes had a length L (along y) and were separated by a gap g. Although not strictly required, such a symmetric configuration can be adopted also in the TO case for increased heating uniformity and tunability, as discussed in what follows.

The different control mechanisms underpinning EO and TO devices imply different wirings (of otherwise identical electrode geometries) as highlighted in Fig. 1a-b. In the TO case, the electrical control consists of the total injected current, which is equally split between the side-electrodes (Fig. 1a). The electrodes are used as resistive elements, acting as microheaters upon current injection, which leads, by means of the Joule effect, to the dissipation of an electrical power $\mathcal{P}=RI^2$. The geometrical parameters of the electrodes were chosen so to yield a resistance $R \sim 60$ Ω, for negligible electrical power dissipation in the contact pads. In the EO case (Fig. 1b), the electrical control signal consists of the applied voltage ($\mathcal{V}$). The electrodes are used as plates of a capacitor whereby the voltage difference applied across the gap g allows to tune the effective index n_{eff} of the relevant (TE_{00}) optical waveguide mode, by accessing the Pockels effect of LN, as described later (equation (2)).

The waveguide section comprised between the electrodes included integrated phase-shifted Bragg grating (PSBG) structures, embedded in the TFLN photonic circuits layer to locally monitor the electrically-induced optical index changes. All the optical structures, encompassing TFLN rib waveguides, PSBGs and integrated fiber-couplers were simultaneously defined by a single lithographic patterning and etching of the TFLN chips, according to the fabrication method described in previous work [33], [35]. The design patterns were first imprinted into a negative resist layer (maN2400) by electron beam exposure (Raith Voyager, 50 kV) then transferred to a chromium hard mask by Cl₂/O₂ reactive ion etching (Oxford PlasmaLab 100) which was finally used to pattern the underlying TFLN layer by Ar⁺ milling (Oxford PlamaLab 100). The EO and TO electrodes were subsequently fabricated to the sides of the waveguides by lift-off (PMMA MicroChem 950) of thermally evaporated (Edwards Auto 306 HV) metal layers consisting of 10 nm of chromium and 50 nm of gold.
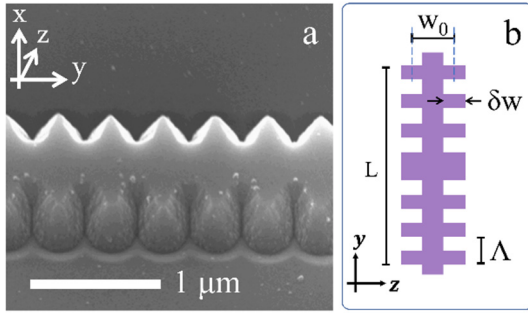
Fig. 2. (a): SEM image of an integrated Bragg reflector in lithium niobate. (b): schematic of the device highlighting the grating period Λ, the waveguide modulation depth δw and its average width w_0. L is the total length of the device. x, y and z are the LN crystal axes.
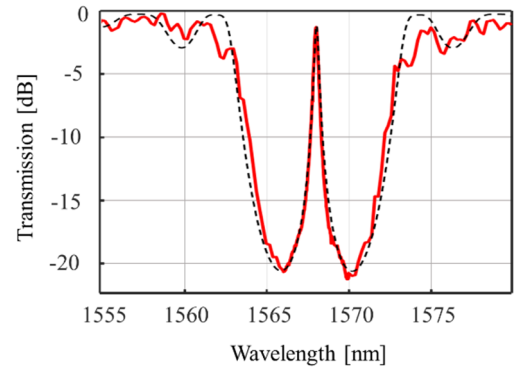

Fig. 3. Transmission spectrum of a π-PSBG in a TFLN rib waveguide etched 360 nm in a 500 nm-thick X-cut LN film, with: $\Lambda = 435$ nm, $\delta w = 230$ nm, $w_0 = 450$ nm, $L = 217.5$ μm. Solid red line: experiments. Dashed line: simulations.

All chips were finally spun with a 2μm-thick PMMA cladding layer.

III. INTEGRATED PSBG SENSING ELEMENT

To monitor in-situ the electrically-induced index change δn_{eff} inside the TFLN nanophotonic circuits, we took advantage of the extreme sensitivity achievable by integrated π-phase-shifted Bragg grating (π-PSBG) structures realized by modulating the sidewalls of a photonic nanowire waveguide (Fig. 2) [33].

The π-PSBG structure, sketched in Fig. 2b, consists of two Bragg grating sections of period Λ, separated by a segment of length $\Lambda/2$, which adds a phase shift of π between the forward- and backward- propagating waves. This creates a narrowband transmission peak (with engineerable bandwidths between 15 pm and 1 nm [33]) inside the larger rejection band (typically 5-10 nm) of the Bragg grating.

Figure 3 shows the typical response of a π-PSBG with data from experiments (solid red line) alongside simulations (black dashed line, based on the model of Ref. [33]) in a passive TFLN device. The spectral position of the narrowband transmission peak coincides with the grating Bragg wavelength, which is linked to the period of the gratings and the effective index (n_{eff}) of the (z-polarized) TE_{00} mode in the waveguide under study:

$$\lambda_{Bragg} = 2\Lambda n_{eff} \qquad (1)$$

In light of the above relationship, the π-PSBG sensor provides an effective means to access extremely small changes in the optical index (δn_{eff}) via optical measurements of the ensuing wavelength-shifts ($\delta\lambda$) of the transmission peak.

Optimized designs for critically coupled devices in state-of-the-art TFLN waveguides can yield bandwidths below 15 pm for the π-PSBG transmission peak [33], which, in combination with its steep spectral edges, grants measurement resolutions in the order of 1 pm in the value of $\delta\lambda$. This results in refractive index sensitivities of one part per million. For this study we implemented integrated π-PSBG designs with modulation periods Λ between 420 nm and 435 nm, in TFLN rib waveguides of width $w_0 = 600\text{-}640$nm, a rib height $h \sim 300$nm, sidewall modulation depths $\delta w = 100\text{-}150$nm

on 500 nm-thick LNOI, yielding $\lambda_{\text{Bragg}} \sim 1540$ nm at room temperature in the passive devices. Such a working point allowed routine optical measurements using standard tunable telecom sources to be performed for real-time retrieval of the waveguide spectral response under the application of the low-frequency TO and EO electrical controls.

IV. ELECTRO- AND THERMO- OPTIC RESPONSE

The EO and TO responses were systematically compared with in-situ optical characterizations performed by coupling light into the TFLN waveguides through broadband grating couplers using single-mode optical fibers. On the detection side we used an InGaAs power meter (Newport 2931-C) synchronized with a tunable external cavity diode laser (Yenista T100S). The DC electrical controls for the experiments were provided by a low-noise benchtop electrical power supply (Keithley 2231A-30-3). The experimental data were further analyzed by Lorentzian fits of the measured PSBG transmission peaks, to identify more accurately the resonance wavelength and assess its shift under the application of a DC electrical bias.

A. Spectral Analysis

In what follows we shall concentrate on the analysis of the shift of the π-PSBG resonance peak under the application of electrical controls, as exemplified by Figure 4 for the case of TO tuning in a TFLN waveguide with $w_0 = 600$nm, $\delta w = 150$nm, $\Lambda = 430$ nm, $L = 215$ μm. The π-PSBG transmission peak, originally located at 1541.37 nm in the passive device (yellow curve), shifts by 1.31 nm upon dissipation of an electrical power $\mathcal{P} = 423$ mW.

The data in Fig. 4 refer to the case where only one microheater is used. The tunability depends only on the local temperature, hence no substantial difference in the refractive index change is to be expected when using only one heater or both, provided that the same electrical power $\mathcal{P}$ is dissipated in the vicinities of the waveguide. This hypothesis was experimentally verified by wiring a specific device in such a way to be able to operate it with both heaters on or with only one. In the former and latter case, the measured
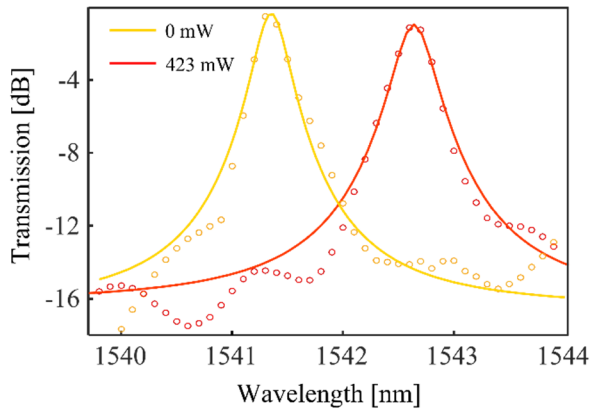
Fig. 4. Transmission peak of a π-PSBG in a passive device (in yellow, $\mathcal{P} = 0$) and with a TO control power $\mathcal{P} = 423$mW (in red). Markers: experimental result. Solid line: Lorentzian fits.
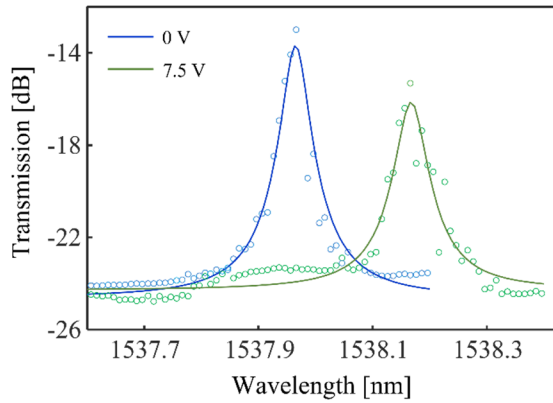

Fig. 5. Transmission spectra of a π-PSBG. The blue circles show the result for the passive device. The peak lies at 1538nm. The green circles show the peak when applying 7.5V, the resonance is red shifted of about 190pm. A Lorentzian fit is superimposed on each peak.

peak shift amounted to 3.01 and 2.93 nm/W, respectively. The difference between the two results can be ascribed to the different wirings of the two resistors and falls well within the measurement uncertainties, confirming the validity of the original assumption. On the other hand, having two microheaters per waveguide offers the important advantage of doubling the operational range delivering twice the total electrical power $\mathcal{P}$ to heat a given waveguide, before reaching the maximum current density tolerated by each resistor. The symmetric two-heater configuration is therefore to be preferred, as it augments the tunability range and reduces the probability of degrading the heating element. Accordingly, in what follows, all TO versus EO device comparisons will be made considering the dual-heater regime of operation (Fig. 1b).

The electro-optic tunability is illustrated by Figure 5, plotting the π-PSBG transmission peak measured without electrical bias (blue curve) together with the one recorded under the application of a static voltage $\mathcal{V} = 7.5$V (green curve) in a TFLN waveguide with $w_0 = 640$nm, $\delta w = 100$nm, $\Lambda = 420$, $L = 680$ μm and $g = 4$ μm. In this case, the PSBG resonance peak, originally centered at 1538 nm is red-shifted by 190 pm.

In the EO case, the Bragg wavelength can be red- or blue- shifted with respect to the resonance of the passive

device changing the voltage polarity. This is peculiar to the EO response and stems from the relationship between the externally applied electric field (E_z) and the index change, given by [36]:

$$\delta n = -\frac{1}{2}n_e^3 r_{33} E_z \qquad (2)$$

where E_z is positive or negative, depending on its orientation with respect to the crystallographic z axis of the LN film. Equation (2), under the simplifying assumption of the EO device acting a double plate dielectric capacitor, allows also to infer a linear dependence of the EO refractive index change on the applied voltage, which was confirmed by further experimental investigations as well as by refined simulations as discussed in the next section.

B. Electrical Tunability

The outcomes of multiple runs of device fabrication, optical characterizations and spectral analyses under varying electrical biases are summarized in Figure 6. Experimental data points (circles) for the wavelength shift of the PSBG resonance ($\delta\lambda$, vertical axis on the right) and the corresponding refractive index change (δn_{eff}, vertical axis on the left) inferred through equation (1), are plotted as a function of the electrical excitation. The latter corresponds to the electrical power $\mathcal{P}$ dissipated in the microheaters and to the voltage $\mathcal{V}$ applied across the side electrodes, in the case of TO and EO devices, respectively. The dashed lines in each plot are linear fits of δn_{eff} versus the two electrical control parameters, varying in the range $\mathcal{P} \in [0, 340]$ mW and $\mathcal{V} \in [0, 28]$ V. From such fits on the experimental data one can extract electrical tunabilities of the optical response amounting to $\sigma^{\text{TO}} = \partial n_{\text{eff}}/\partial\mathcal{P} = 3.6 \times 10^{-3}$ W^{-1} ($\partial\lambda/\partial\mathcal{P} = 3.01$ nm/W) and $\sigma^{\text{EO}} = \partial n_{\text{eff}}/\partial\mathcal{V} = 3 \times 10^{-5}$ V^{-1} ($\partial\lambda/\partial\mathcal{V} = 25.2$ pm/V) for the TO and EO cases, respectively.

The TO and EO effect exhibit unipolar and bipolar tuning, respectively, with respect to the passive device ($\delta\lambda = 0$). The EO tuning shows almost perfect agreement with the linear law expected from equation (2). Moreover, the tunability value extrapolated from the experiments (σ^{EO}) matches very well also the outcome of further refined numerical simulations, using a commercial finite element mode solver (COMSOL Multiphysics). The transvers (x-z) distributions, computed with the latter, of the optical guided modes and of the electric field generated by the side electrodes in the TFLN waveguide are illustrated by the inset of Fig. 6b. Equivalent numerical investigations, taking into account the specific TFLN waveguide and electrode geometries of the experiments were also developed to design and analyze the results for TO devices. An example is provided in the inset of Fig. 6a. Based on literature values for the thermo-optic dependence of the refractive indices of congruent LN [34] and of the cladding materials, the x-z temperature profile is converted into transverse refractive index distributions to be used as inputs to commercial mode solvers to determine the values of n_{eff} as a function of power, for direct comparisons with the data of Fig. 6a. Furthermore, the same simulation tools were employed to use the PSBG as a thermometer, to locally monitor the temperature inside TFLN
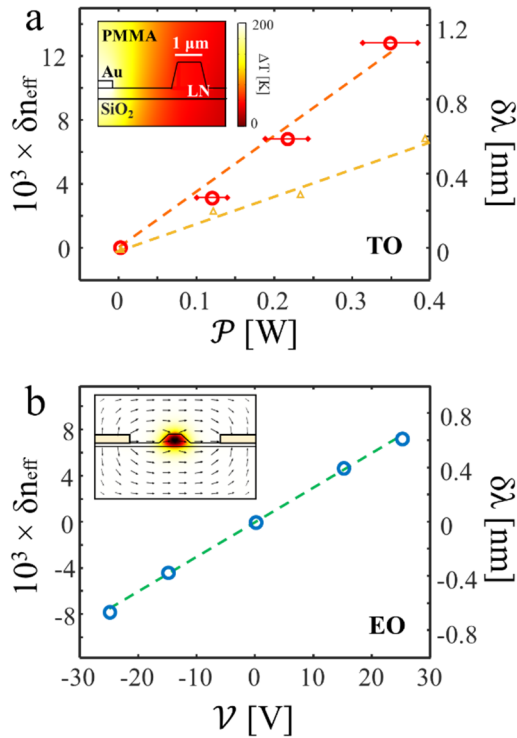
Fig. 6. Variation of the waveguide effective index δn_{eff} (and resonance shift $\delta\lambda$) as a function of: (a) TO control power ($\mathcal{P}$) and (b) EO control voltage ($\mathcal{V}$). Circles: Experimental data in devices with g = 5μm for the TO case and 4μm for the EO case. Dashed lines: linear fits. In insets: COMSOL simulation of (a) the thermal field and (b) the electrostatic and optical field distribution. The triangles and the associated linear fit in (a) quantify the TO crosstalk from the nearest waveguide, 65 μm away from the one under study.

waveguides. As an example, for $\mathcal{P} = 340$ mW ($\delta\lambda = 1$ nm) in Fig. 6a, the estimated waveguide temperature increase is $\delta T = 55$ °C.

C. Cross-Talk

Another important parameter to consider when assessing the device performance is the crosstalk among adjacent devices. This may set the ultimate limit in implementing the active control of different waveguides densely packed in integrated photonic circuits, preventing to fully leverage the low-footprint of TFLN nanophotonics.

Crosstalk effects were essentially absent for our EO devices, since the simple existence of grounded metal trenches (required to apply the control voltage across each waveguide) has an electric shielding effect on neighboring devices spread on the same chip. Thermal crosstalk can instead quickly become a significant issue for TO devices in highly integrated optical circuits, motivating the adoption of additional measures for thermal isolation [14], [30]. This however comes at the price of considerable complications in the fabrication process and imposes further requirements for vacuum operation in extreme cases [37]. It is therefore relevant to investigate crosstalk limitations also in the context of TFLN.

In our case the spatial separation (along z) between adjacent waveguides was set to a fixed value, $s = 65$ μm and no extra measure (e.g. additional trench fabrication) was implemented for thermal isolation. The thermal crosstalk was investigated

by injecting different currents in the heaters of the first, the second, and the third waveguide of the same set (with the above spacing), while monitoring the output of the fourth waveguide. We then tested the actual tunability of the latter (with its own TO control). The results of the direct tunability and the crosstalk from the nearest-neighbor waveguide, are shown in Figure 6a as circles and triangles, respectively, alongside with linear fits on the two sets of experimental data point represented by the markers. From the plots it is apparent that the slope of the cross-talk line among nearest neighbor waveguides (triangles) is approximately half the one of the thermal tunability of the waveguide under test (circles), approximately 1.5 vs 3 nm/W. The measured cross talk for the second and third nearest neighbors is comparable to the one shown for the nearest neighbor in Figure 6a, showing a relatively slow decay of the thermal distribution over spatial scales beyond 65 μm. The cross-talk could be reduced by improving the heat dissipation from the Silicon substrate of our chip (e.g. mounting it on a heatsink).

D. Electrode-Gap Versus Tunability Tradeoff

Another critical tradeoff, especially for EO designs, concerns the impact of the metal electrodes on optical waveguide losses. As shown by the diagram of Fig. 7a, the electrodes introduce an additional loss term to the optical field propagation in the TFLN waveguide, which decreases as the electrode gap g is increased. The long-range action of the thermal distributions across the device (cf section III-C) allows to target designs with larger electrode gaps for the TO devices, without significantly affecting their electrical-to-optical tunability σ^{TO}. This is confirmed by the experimental data shown in Fig. 7b (red circles). Considering electrode gaps of 4, 5 and 6.5 μm, the TO tunability of the effective index does not show a clear trend. The fluctuations seen in the experimental data points are to be ascribed to the fabrication imperfections introduced by different wiring of the various microheaters, rather than being an indicator of a significant impact of the gap for the TO tunability. This is consistent with the more intuitive insight (confirmed by simulations) indicating that, provided that the area in the vicinity of the waveguide reaches the working temperature, the refractive index is essentially uniform within the electrode gap.

The symmetric configuration, in this sense, is most helpful in ensuring that the waveguide sees no temperature gradient, allowing similar performances across a wider range of gaps. This permits to implement gaps larger than 4μm (where no additional insertion losses induced by electrode proximity were observed in the experiments), without compromising the tunability σ^{TO}.

The situation appears different for the EO devices. The experimental data (blue circles) in Figure 7b highlight a significant decrease in the tunability σ^{EO} for increasing gap sizes, matching relatively well a linear fit with a negative slope, in the range between 3 and 6 μm (dashed line). This is in full agreement with the predictions of numerical simulations and with the expected spatial scales for the decay of the electrical field amplitude in the guiding layer as the electrode gap is
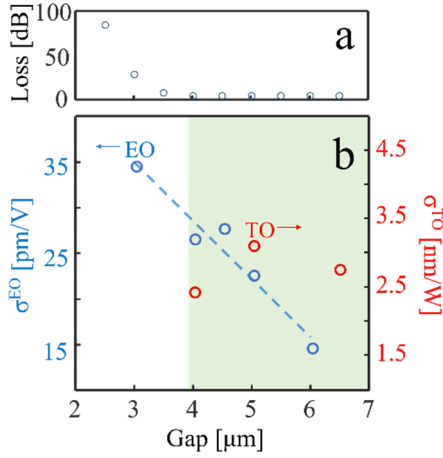
Fig. 7. (a) Simulation of evolution of the extra loss (in dB) induced by the metal electrodes on the guided TE_{00} mode as a function of the gap g for a device of length 250μm. (b) EO (blue) and TO (red) tunabilities σ^{EO} (left axis) and σ^{TO} (right axis), respectively, plotted as a function of the electrode gap. Circles: experiments. Dashed line: Linear fit on the EO data. The shaded area highlights the region where the extra optical losses were experimentally found to be negligible.

increased. The electrode-induced losses therefore appear as a key limiting factor for the maximum achievable tunability of EO devices. Setting the gap between the electrodes to the minimum allowed value to avoid extra losses, i.e. $g = 4\text{-}5\ \mu$m, results in the tunability value of $\sigma^{EO} \sim 25$ pm/V, quoted for Fig. 6b.

E. Maximum Index Modulation

The upper limit to the index modulation (wavelength shift) achievable in the case of EO devices is ultimately set by the maximum value of the electric field that can be safely applied without dielectric breakdown or ferroelectric domain inversion. Given the value of the coercive field in congruent LN ($E_c = 21$ kV/mm), the maximum applicable external voltage (for $g = 4\ \mu$m) is then $\mathcal{V}_{max} \sim 80$ V, corresponding to a maximum index modulation $\delta n_{max} \sim 4.8 \times 10^{-2}$ ($\delta\lambda_{max} \sim 4$ nm), extrapolated from the data of Fig. 6.

The maximum achievable wavelength shift for the TO devices is instead limited by the maximum current that a single heating electrode can tolerate. In our case this amounts typically to $I_{max} \sim 75$mA, corresponding to a maximum power $\mathcal{P}_{max} = 400$ mW per heater. Accordingly, the extrapolated maximum index modulation achievable with TO controls is $\delta n_{max} \sim 2.8 \times 10^{-2}$ ($\delta\lambda_{max} \sim 2.4$ nm), approximately half of the EO value. However it is worth underlining that the goal of this paper was to compare the performance of EO and TO tunability under identical device architectures and electrodes suited for both operating conditions. As a consequence the fabrication conditions of our heaters were not optimized so to maximize their critical current density (by e.g. implementing thicker resistors or using higher resistivity materials), which is instead a viable avenue to further push device performance [30].
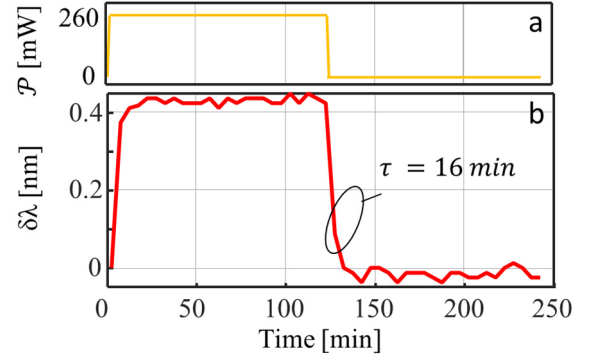

Fig. 8. TO long-term stability measurements. (a) Applied control waveform (dissipated power $\mathcal{P}$). (b) Resulting time-evolution of the TO wavelength shift ($\delta\lambda$) which reaches the target value after a few minutes of thermalization. Fluctuations are mainly due to coupling instability.

F. Stability

This final section is devoted to experiments addressing long-term stability issues of the EO and TO devices, which is particularly critical for quasi-static regimes of operation.

Figures 8 and 9 present the results of the stability analysis performed on two representative devices for the TO and the EO case, respectively. The working point for the former was set to a power $\mathcal{P} = 260$ mW, leading to a wavelength shift $\delta\lambda = 416$ pm. Measurements for the EO involved applying a voltage $\mathcal{V} = \pm 28$ V, corresponding to an expected wavelength shift $\delta\lambda = \pm 410$ pm (for this specific device $\sigma^{EO} = 14.7$pm/V), and then monitoring the spectral location of the PSBG resonance every five minutes over a period of two hours. The values were chosen to be in both cases well within the limits of the device tunability.

The case of TO devices is illustrated by Figure 8. Figure 8a shows the quasi-static control waveform of the dissipated power. From Figure 8b it is apparent that in this case the peak shift remains basically constant for the whole time (120 min) over which the control current is injected in the heaters and then goes back to zero with a time constant of 16 min. The residual oscillations visible in the time traces of the wavelength shift $\delta\lambda$ are comparable with the experimental uncertainties, due mainly to instabilities in the fiber coupling over long measurements. This however leaves the peak transmission values unaffected.

The case of EO is illustrated by Figure 9. Fig. 9a shows the control waveform $\mathcal{V}$ applied to the EO device and Fig. 9b is the resulting EO response, monitored by following the evolution of the wavelength shift $\delta\lambda$ over time. From the latter, it is apparent that, after reaching the expected value (highlighted by the dashed horizontal line in Fig. 9b), the measured wavelength overshoots it ($\delta\lambda > 410$ pm), before experiencing a progressive blue-shift which tends to bring it back towards the value at rest ($\delta\lambda \rightarrow 0$) over a longer time scale, despite the continued application of the bias at $\mathcal{V} = 28$ V.

When the external field is switched off, the wavelength does not immediately return to the value at rest, but rather converges slowly to it, with a time constant of the order of $\sim$70 minutes. A qualitatively similar behavior is observed for negative voltages ($\mathcal{V} = -28$ V), albeit with somewhat
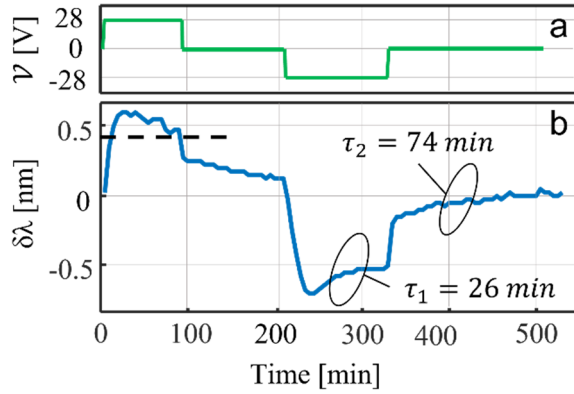
Fig. 9. EO long-term stability measurement. (a) Quasi-static control waveform (applied voltage). (b) Resulting time evolution of the wavelength shift $\delta\lambda$. After turning $\mathcal{V}$ on, $\delta\lambda$ reaches and exceeds the target value (dashed line) before experiencing a slow blue drift. Similar slow drifts are also visible when turning the voltage off and reversing the voltage polarity.

different time constants and limited wavelength shift reproducibility over multiple cycles of operation (not shown here). The effects are characteristic signatures of the DC drift, typically affecting LN under the application of external static electric field [25], [26].

V. CONCLUSION

We reported a comparative experimental study of thermo-optically and electro-optically tuned nanophotonic devices in x-cut thin film LiNbO₃, considering relevant performance indicators for the tuning and re-configurability of photonic integrated circuits implemented on this platform. By leveraging the high sensitivity of engineered Bragg grating structures embedded in photonic nanowire waveguides, we systematically analyzed the tunability, crosstalk and stability of the EO and TO controls over the effective index of the TE_{00} guided-modes at telecom wavelengths. Using identical device designs and fabrication processes, the index tunability in TO and EO modes of operation was experimentally assessed to be 3.6×10^{-3} W^{-1} and 3×10^{-5} V^{-1}, respectively. Moreover, with a combination of experiments and numerical simulation we could identify critical factors for the design of EO devices, concerning the optimal distance between the control electrodes ($\sim$4 μm), as well as for TO devices, concerning the spacing among neighboring devices (quantifying the thermal crosstalk for distances above 50 μm). The ultimate limits to the achievable driving voltages and powers of this material platform yield comparable values for the maximum index modulation of TO and EO configurations, estimated to be $\delta n_{max} \sim 2.8 \times 10^{-2}$ and $\sim$4.8 $\times 10^{-2}$, respectively. Finally, tests of the long-term stability of the two different tuning strategies, confirmed that devices relying on TO reconfigurability could be stably tuned for many hours, whereas the EO response recorded under similar operating conditions is critically affected by erratic DC-drifts, similarly to what observed in tradition LN devices [25], [26].

The results of the study allow to critically assess the suitability of two complementary approaches for tuning PICs in thin film LiNbO₃, in relationship to the broad range of emerging

linear, nonlinear and quantum optics applications of this important nanophotonic platform. They can be advantageously used to make informed choices at design and fabrication level and eventually resort to further refined solutions to best match the performance requirements of specific applications areas. The peculiarities of the EO response of TFLN waveguides make them ideal for applications requiring fast modulation, high integration densities and low consumption, encompassing also cryogenic PIC operation, to be specifically addressed by future investigations. However, particular caution is to be taken to counteract, at design, fabrication and operation level [25], [26] the deleterious effect of long-term DC drifts. TO effects on the other hand provide a reliable mechanism for mode index control, granting stability over long time scales and well-suited also for periodically poled devices. Such advantageous features are to be traded against the need for less densely packed PICs and for higher on-chip power dissipation, associated to TO operation. All those considerations are of the utmost importance for practical implementations of advanced PICs in LiNbO₃, leveraging its outstanding potential for advanced quantum and nonlinear optics applications, afforded by the unique properties of this material in combination with the ultralow footprints and power consumption, as well as advanced functionalities afforded by nanophotonic circuits for signal synthesis, processing and computation bridging the electrical and optical domains.

REFERENCES

[1] P. Cheben, R. Halir, J. H. Schmid, H. A. Atwater, and D. R. Smith, "Subwavelength integrated photonics," *Nature*, vol. 560, pp. 565–572, Aug. 2018.

[2] W. Bogaerts and L. Chrostowski, "Silicon photonics circuit design: Methods, tools and challenges," *Laser Photon. Rev.*, vol. 12, no. 4, Apr. 2018, Art. no. 1700237.

[3] G. Zhang et al., "An integrated silicon photonic chip platform for continuous-variable quantum key distribution," *Nature Photon.*, vol. 13, pp. 839–842, Aug. 2019.

[4] J. Wang, F. Sciarrino, A. Laing, and M. G. Thompson, "Integrated photonic quantum technologies," *Nature Photon.*, vol. 14, no. 5, pp. 273–284, May 2020.

[5] W. Bogaerts et al., "Programmable photonic circuits," *Nature*, vol. 586, no. 7828, pp. 207–216, Oct. 2020.

[6] B. J. Shastri et al., "Photonics for artificial intelligence and neuromorphic computing," *Nature Photon.*, vol. 15, pp. 102–144, Feb. 2021.

[7] M. Milanizadeh et al., "Separating arbitrary free-space beams with an integrated photonic processor," *Light Sci. Appl.*, vol. 11, pp. 1–12, Jul. 2022.

[8] D. Marpaung, J. Yao, and J. Capmany, "Integrated microwave photonics," *Nature Photon.*, vol. 13, no. 2, pp. 80–90, Feb. 2019.

[9] X. Xue et al., "ROTOS: A reconfigurable and cost-effective architecture for high-performance optical data center networks," *J. Lightw. Technol.*, vol. 38, pp. 3485–3494, Jul. 1, 2020.

[10] E. Toninelli et al., "Concepts in quantum state tomography and classical implementation with intense light: A tutorial," *Adv. Opt. Photon.*, vol. 11, pp. 67–134, Mar. 2019.

[11] A. A. S. Falah, M. R. Mokhtar, Z. Yusoff, and M. Ibsen, "Reconfigurable phase-shifted fiber Bragg grating using localized micro-strain," *IEEE Photon. Technol. Lett.*, vol. 28, no. 9, pp. 951–954, May 1, 2016.

[12] W. Zhang and J. Yao, "A fully reconfigurable waveguide Bragg grating for programmable photonic signal processing," *Nature Commun.*, vol. 9, no. 1, pp. 1–9, Apr. 2018.

[13] G. T. Reed, G. Mashanovich, F. Y. Gardes, and D. J. Thomson, "Silicon optical modulators," *Nature Photon.*, vol. 4, pp. 518–526, Jul. 2010.

[14] F. Ceccarelli, S. Atzeni, A. Prencipe, R. Farinaro, and R. Osellame, "Thermal phase shifters for femtosecond laser written photonic integrated circuits," *J. Lightw. Technol.*, vol. 37, no. 17, pp. 4275–4281, Sep. 1, 2019.

[15] E. L. Wooten et al., "A review of lithium niobate modulators for fiber-optic communications systems," *IEEE J. Sel. Top. Quantum Electron.*, vol. 6, pp. 69–82, Jan. 2020.

[16] B. Desiatov, A. Shams-Ansari, M. Zhang, C. Wang, and M. Lončar, "Ultra-low-loss integrated visible photonics using thin-film lithium niobate," *Optica*, vol. 6, no. 3, pp. 380–384, Mar. 2019.

[17] M. Zhang, C. Wang, P. Kharel, D. Zhu, and M. Lončar, "Integrated lithium niobate electro-optic modulators: When performance meets scalability," *Optica*, vol. 8, pp. 652–667, May 2021.

[18] D. Pohl et al., "100-GBd waveguide Bragg grating modulatorin thin-film lithium niobate," *J. Lightw. Technol.*, vol. 33, pp. 85–88, Jan. 1, 2021.

[19] M. He et al., "High-performance hybrid silicon and lithium niobate Mach–Zehnder modulators for 100 Gbit s^{-1} and beyond," *Nature Photon.*, vol. 13, pp. 359–364, May 2019.

[20] M. Li, J. Ling, Y. He, U. A. Javid, S. Xue, and Q. Lin, "Lithium niobate photonic-crystal electro-optic modulator," *Nature Commun.*, vol. 11, no. 1, pp. 1–8, Aug. 2020.

[21] T. Park et al., "High-efficiency second harmonic generation of blue light on thin-film lithium niobate," *Opt. Lett.*, vol. 47, pp. 2706–2709, Jun. 2022.

[22] E. Lomonte et al., "Single-photon detection and cryogenic reconfigurability in lithium niobate nanophotonic circuits," *Nature Commun.*, vol. 12, pp. 1–10, Nov. 2021.

[23] D. Zhu et al., "Integrated photonics on thin-film lithium niobate," *Adv. Opt. Photon.*, vol. 13, pp. 242–352, Jun. 2021.

[24] A. Boes, B. Corcoran, L. Chang, J. Bowers, and A. Mitchell, "Status and potential of lithium niobate on insulator (LNOI) for photonic integrated circuits," *Laser Photon. Rev.*, vol. 12, no. 4, Apr. 2018, Art. no. 1700256.

[25] J. P. Salvestrini, L. Guilbert, M. Fontana, M. Abarkan, and S. Gille, "Analysis and control of the DC drift in LiNbO3 based Mach–Zehnder modulators," *J. Lightw. Technol.*, vol. 29, no. 10, pp. 1522–1534, May 1, 2011.

[26] C. Gee, G. Thurmond, H. Blauvelt, and H. Yen, "Minimizing DC drift in LiNbO$_3$ waveguide devices," *Appl. Phys. Lett.*, vol. 47, pp. 211–213, Aug. 1985.

[27] M. Spagnolo et al., "Experimental photonic quantum memristor," *Nat. Photonic*, vol. 16, pp. 318–323, Apr. 2022.

[28] F. Lenzini et al., "Integrated photonic platform for quantum information with continuous variables," *Sci. Adv.*, vol. 4, Dec. 2018, Art. no. eaat9331.

[29] S. Sun et al., "Bias-drift-free Mach–Zehnder modulators based on a heterogeneous silicon and lithium niobate platform," *Photon. Res.*, vol. 8, pp. 1958–1963, Dec. 2020.

[30] X. Liu et al., "Highly efficient thermo-optic tunable micro-ring resonator based on an LNOI platform," *Opt. Lett.*, vol. 45, pp. 6318–6321, Nov. 2020.

[31] M. Xu et al., "High-performance coherent optical modulators based on thin-film lithium niobate platform," *Nature Commun.*, vol. 11, pp. 1–7, Aug. 2020.

[32] Y. Hu et al., "On-chip electro-optic frequency shifters and beam splitters," *Nature*, vol. 599, pp. 587–593, Nov. 2021.

[33] A. Prencipe, M. A. Baghban, and K. Gallo, "Tunable ultranarrowband grating filters in thin-film lithium niobate," *ACS Photon.*, vol. 8, no. 10, pp. 2923–2930, Sep. 2021.

[34] G. J. Edwards and M. Lawrence, "A temperature-dependent dispersion equation for congruently grown lithium niobate," *Opt. Quantum Electron.*, vol. 16, no. 4, pp. 373–375, Jul. 1984.

[35] M. A. Baghban, J. Schollhammer, C. Errando-Herranz, K. B. Gylfason, and K. Gallo, "Bragg gratings in thin-film LiNbO$_3$ waveguides," *Opt. Exp.*, vol. 25, pp. 32323–32332, Dec. 2017.

[36] A. Yariv and P. Yeh, *Photonics: Optical Electronics in Modern Communications*. Oxford, U.K.: Oxford Univ. Press, 2007, pp. 450–458.

[37] F. Ceccarelli, S. Atzeni, C. Pentangelo, F. Pellegatta, A. Crespi, and R. Osellame, "Low power reconfigurability and reduced crosstalk in integrated photonic circuits fabricated by femtosecond laser micromachining," *Laser Photon. Rev.*, vol. 14, no. 10, Oct. 2020, Art. no. 2000024.

Alessandro Prencipe received the B.S. and M.S. degrees in engineering physics from Politecnico di Milano, Italy, in 2016 and 2018, respectively. He is currently pursuing the Ph.D. degree with the Department of Applied Physics, KTH Royal Institute of Technology, Stockholm, Sweden. His research interest mainly focuses on the design, fabrication, and characterization of optical circuits in thin film lithium niobate.

Katia Gallo received the M.Sc. degree in electronic engineering from Roma "La Sapienza", the Ph.D. degree in electronic engineering from Palermo University, and the Ph.D. degree in physics from the University of Nice Sophia-Antipolis. She led the research line on LiNbO3 integrated optical devices at the Optoelectronics Research Centre, Southampton, prior to joining the Royal Institute of Technology, Sweden, in 2007, where she currently holds a Professor position at the Department of Applied Physics and Heading the Nonlinear and Quantum Photonics Group. Her research interests span theory, technology, and experiments in nanostructured ferroelectrics and integrated nonlinear optical devices, with a focus on all-optical signal processing and quantum and bio-photonics applications. In Sweden, she coordinates the VR Consortium for optical quantum sensing and the Quantum Communications Pillar, Wallenberg Centre for Quantum Technology. She has authored more than 150 journals and conference contributions and given 33 invited talks at international conferences and symposia in the fields of nonlinear optics, polar dielectric materials, laser physics, and optical telecommunications. She was a recipient of the 1996 Italy IEEE Student Award in electronic engineering and the Fellowships from the EU, the Leverhulme Trust, the London Technology Network, and the Swedish Research Council, France, U.K., and Sweden.